ADVANCED MATERIALS
www.advmat.de

Joint Charge Storage for High-Rate Aqueous Zinc–Manganese Dioxide Batteries

Yan Jin, Lianfeng Zou, Lili Liu, Mark H. Engelhard, Rajankumar L. Patel, Zimin Nie, Kee Sung Han, Yuyan Shao, Chongmin Wang, Jia Zhu, Huilin Pan, and Jun Liu**

Aqueous rechargeable zinc–manganese dioxide batteries show great promise for large-scale energy storage due to their use of environmentally friendly, abundant, and rechargeable Zn metal anodes and MnO_2 cathodes. In the literature various intercalation and conversion reaction mechanisms in MnO_2 have been reported, but it is not clear how these mechanisms can be simultaneously manipulated to improve the charge storage and transport properties. A systematical study to understand the charge storage mechanisms in a layered δ-MnO_2 cathode is reported. An electrolyte-dependent reaction mechanism in δ-MnO_2 is identified. Nondiffusion controlled Zn^{2+} intercalation in bulky δ-MnO_2 and control of H^+ conversion reaction pathways over a wide C-rate charge–discharge range facilitate high rate performance of the δ-MnO_2 cathode without sacrificing the energy density in optimal electrolytes. The Zn-δ-MnO_2 system delivers a discharge capacity of 136.9 mAh g^{-1} at 20 C and capacity retention of 93% over 4000 cycles with this joint charge storage mechanism. This study opens a new gateway for the design of high-rate electrode materials by manipulating the effective redox reactions in electrode materials for rechargeable batteries.

With the rapid development of renewable energy such as wind and solar, the low cost and high power energy storage technologies become important for the reliability of the electric grid systems to accommodate peak-electricity integration.[1–6] The electrochemical capacitors, basically with relatively low cost, can store energy in seconds with high power density but low energy density.[7–11] Therefore, it is highly desired to pursue alternative energy storage solution enabling both high energy densities and high power densities.[12,13] In recent years, the mild aqueous Zn-based batteries have attracted increasing interest because of the low cost and high capacity of Zn metal anode (819 mAh g^{-1}), suitable redox potential (–0.76 V vs standard hydrogen electrode), and nonflammability, nontoxicity, and high ionic conductivity of aqueous electrolytes.[14] A few cathode materials such as polymorphs of MnO_2,[15–19] the vanadium-based oxides/sulfides,[20–22] prussian blue analogs,[23,24] cation-deficient spinel $ZnMn_2O_4$,[25] $NaV_2(PO_4)_3$[26] etc., have been investigated for Zn-based batteries. Among them, the MnO_2 cathode has attracted the most interest due to its high capacity (308 mAh g^{-1}), low cost, and the diverse energy storage mechanisms.[16] Different from the widely investigated Li-ion and Na-ion battery systems, the aqueous Zn-MnO_2 batteries exhibit complicated energy storage mechanisms. Zn^{2+} ion intercalation in $\alpha/\gamma/\delta$-MnO_2 forming spinel $ZnMn_2O_4$,[27,28] Zn-buserite,[29] layered and/or tunnel Zn_xMnO_2,[28,30] H^+ reaction in α-MnO_2 nanofiber forming MnOOH,[16] and Zn^{2+} and H^+ cointercalation in akhtenskite-MnO_2 and polymer intercalated layered MnO_2 have been reported in literatures.[15,17] The different observed storage mechanisms have been attributed to various crystal structure and particle size of cathodes of the starting materials, but have been a subject of significant discussion and debate.[17] The lack of detailed understanding and control of the mechanisms have limited the development of more efficient and reliable electrode materials for practical applications.[16]

Among various polymorphs of MnO_2, the layer δ-MnO_2 polymorph exhibits a large interlayer spacing, which could be appealing for high-rate electrochemical performance. Here, we demonstrate that the charge storage mechanism in rechargeable aqueous Zn-MnO_2 batteries with layered δ-MnO_2 as cathode material can be systematically manipulated to produce optimum high rate electrochemical properties and long cycle life. Combining detailed crystal phase, morphology evolution, and electrochemical kinetic studies in δ-MnO_2 cathode, a joint nondiffusion Zn^{2+} ion intercalation in bulk δ-MnO_2 and H^+ conversion reaction were revealed (**Figure 1**). Such joint charge storage reaction in δ-MnO_2 is mainly associated with the

Y. Jin, Dr. R. L. Patel, Z. Nie, Dr. Y. Shao, Dr. H. Pan, Dr. J. Liu
Energy & Environment Directorate
Pacific Northwest National Laboratory
Richland, WA 99354, USA
E-mail: huilin.pan@pnnl.gov; jun.liu@pnnl.gov
Y. Jin, Prof. J. Zhu
College of Engineering and Applied Sciences
Nanjing University
Nanjing 210093, China
Dr. L. Zou, Dr. M. H. Engelhard, Dr. K. S. Han, Dr. C. Wang
Environmental Molecular Sciences Laboratory
Pacific Northwest National Laboratory
Richland, WA 99354, USA
Dr. L. Liu
Physical Sciences Division
Pacific Northwest National Laboratory
Richland, WA 99354, USA
The ORCID identification number(s) for the author(s) of this article can be found under https://doi.org/10.1002/adma.201900567.

DOI: 10.1002/adma.201900567

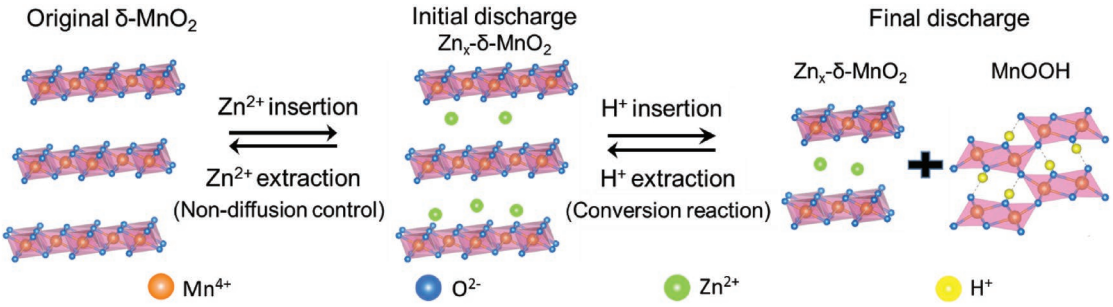

Figure 1. Joint nondiffusion controlled Zn^{2+} intercalation and H^+ conversion reaction mechanism in δ-MnO_2.

electrolyte media for redox reactions but varies with charge–discharge rates. In $Zn(TFSI)_2$-based electrolyte, nondiffusion controlled Zn^{2+} ion storage mechanism dominates the first step fast charge storage in bulk δ-MnO_2 without significant phase transition, while the diffusion controlled H^+ conversion reaction dominates the following step reactions. This joint charge storage mechanism leads to the superior high-rate behavior of aqueous Zn-MnO_2 batteries without sacrificing much of the energy density, showing a high reversible capacity of 136.9 mAh g^{-1} at 20 C and 93% capacity retention after 4000 cycles. This study opens a new approach of designing high-rate, high-energy electrode materials by manipulating the effective redox reactions in electrode materials.

Layered δ-MnO_2 was synthesized for rechargeable aqueous Zn batteries using simple hydrothermal method according to previous report.[31] The crystal structure of δ-MnO_2 is made of loosely bound layers of edge-shared MnO_6 located on the (001) plane (Figure 1). The scanning electron microscopy (SEM) image of the prepared δ-MnO_2 shows hierarchical nanoparticle morphologies with an average diameter of around 500 nm, which consists of small nanoflakes as shown in **Figure 2**a. High-resolution transmission electron microscopy (HRTEM) in Figure 2b reveals the lattice spacing of 0.7 nm for the (001) crystal plane of δ-MnO_2. The crystalline phase of as-prepared sample was further confirmed by X-ray diffraction (XRD), as shown in Figure 2c, which is in good agreement with the structure of layered birnessite δ-MnO_2 (JCPDS: 80-1098).[32]

We first analyzed the redox reactions in layered MnO_2 cathode by identifying the kinetic parameters of δ-MnO_2. **Figure 3**a and Figure S1 of the Supporting Information show the cyclic voltammetry (CV) scanning curves of δ-MnO_2 from 0.1 to 10 mV s^{-1} in 1 M $Zn(TFSI)_2$ with 0.1 M $Mn(TFSI)_2$ electrolyte. Pre-addition of manganese salt in electrolyte was used to suppress Mn^{2+} dissolution from MnO_2 electrodes.[16] Two pairs of redox peaks denoted as peak 1, 2, 3, 4 were observed in δ-MnO_2 during charge and discharge, indicating two potential types of redox reactions. The current (i) of CV scanning is assumed to exhibit a dependency of the sweep rate (v): $i = av^b$,[33,34] where a and b are variable values, and the value b falls in a range of 0.5–1, depending on the charge storage kinetics in δ-MnO_2. The value b of 0.5 suggests that the charge storage in electrode material is controlled by solid-state diffusion of active ions, whereas value b of 1 indicates that the current is surface controlled electrochemical capacitive process in electrode material.[34] (Note that the zinc-based aqueous electrolytes show a high ionic conductivity of > 40 mS cm^{-1} (Table S1, Supporting Information), indicating fast diffusion kinetics of active ions in the electrolyte. The diffusion of active ions in liquid electrolyte is therefore not considered as the rate-limiting step for the overall electrochemical redox reactions in solid δ-MnO_2 electrode. We plotted the dependence curves between log (i) with log (v) for the observed redox peaks, respectively (Figure 3b). The fitted curves for four peaks exhibit two different regions. In the scanning rate range of 0.1–1 mV s^{-1}, the fitting b value is approaching 1 (0.87, 0.81, 0.90, and 0.82 for peak 1 to 4, respectively), which indicates that the kinetics is fast and mainly nondiffusion controlled. In contrast, the value of b decreased to 0.76, 0.73, and 0.64 for peak 1, 3, and 4, respectively in the scanning rate range of 2–10 mV s^{-1} (Note that the fitting curve for peak 2 is not shown because the peak shifted out of the voltage range). This indicates that the electrochemical charge storage in δ-MnO_2 cathode is contributed by both nondiffusion controlled and solid-state ion diffusion controlled reactions within a wide scanning rate range, where

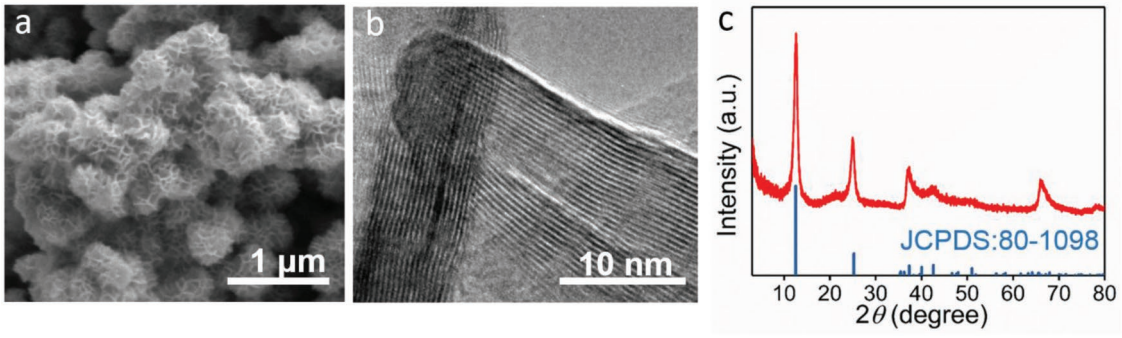

Figure 2. Structural characterization of δ-MnO_2. a) SEM image, b) HRTEM image, and c) XRD data of δ-MnO_2.

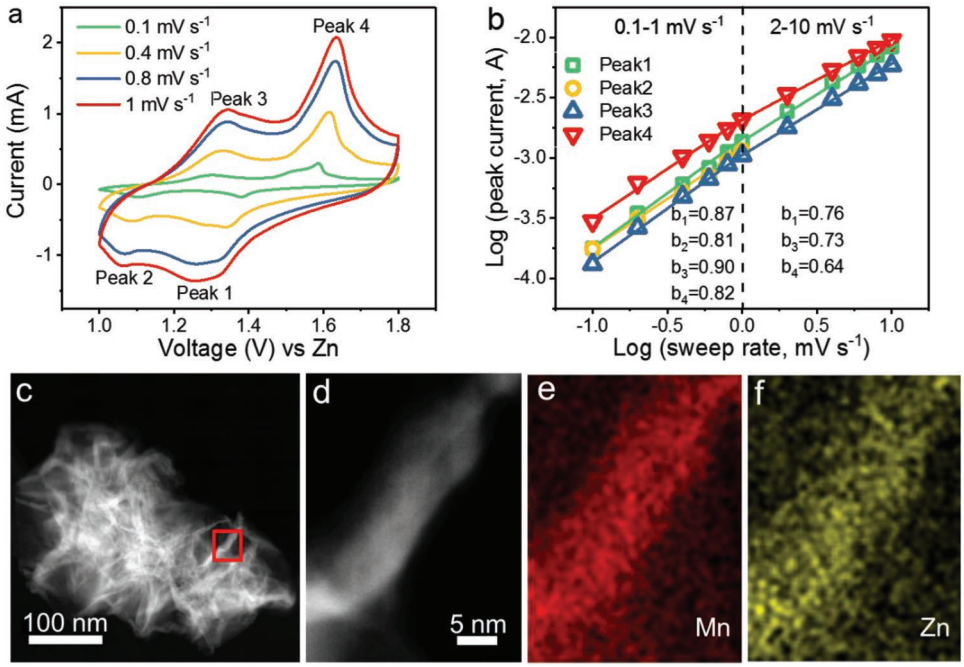

Figure 3. Kinetic analysis of the electrochemical reactions in δ-MnO_2. a) CV curves of Zn-MnO_2 batteries at different scan rates. b) *b*-value determination at each peak according to $i = av^b$ (i is current; v is sweep rate; a, b are variable values). Note the value of b_n (n = 1, 2, 3, 4) indicates the b value of peak n in the CV curves in (a) and Figure S1 (Supporting Information). c–f) STEM-HAADF images (c,d) and STEM–EDS mappings of the elemental distributions of e) Mn and f) Zn for the δ-MnO_2 electrode discharged to 1.43 V in the second cycle in the selected electrode area in Figure 3c. The red rectangular region in Figure 3c is magnified in Figure 3d. Electrolyte: 1 M $Zn(TFSI)_2$ electrolyte with 0.1 M $Mn(TFSI)_2$ additive in water.

the nondiffusion controlled charge storage contributes more effective capacity with a scanning rate lower than 1 mV s^{-1}.

To further quantify the capacity contribution, the correlation between the normalized capacity and $v^{-1/2}$ for δ-MnO_2 was established from sweep rate of 0.2 to 10 mV s^{-1} in Figure S2a of the Supporting Information, where the nondiffusion controlled capacity remains constant, and capacity resulted by solid-state diffusion controlled process varies with $v^{-1/2}$.[10] In excellent agreement of the results in Figure 3b, two regions of capacity for δ-MnO_2 were observed. With v < 1 mV s^{-1}, the normalized charge storage capacity decreases slightly with increasing the sweep rate, whereas the dependence of capacity on sweep rate becomes stronger at v > 1 mV s^{-1}. The critical sweep rate separating diffusion controlled capacity and nondiffusion controlled capacity is likely associated with the intrinsic charge transport properties in the electrode material and used electrolytes. We further quantified the nondiffusion controlled capacity in δ-MnO_2 in the inset of Figure S2a of the Supporting Information, with 76%, 82%, 86%, 85%, and 88% at the sweep rate of 0.2, 0.4, 0.6, 0.8, and 1 mV s^{-1} respectively. In addition, the redox peaks exhibit small voltage offset lower than 50 mV at sweep rate < 1 mV s^{-1} (Figure S2b, Supporting Information), and this is similar to surface redox reactions with fast charge storage kinetics.[33] The nondiffusion controlled capacity should be attributed to the "pseudocapacitance"-like charge storage in δ-MnO_2 cathode in aqueous electrolyte. The STEM–EDS mappings of discharged δ-MnO_2 cathode (1.43 V) in Figure 3c–f revealed the uniform distribution of elemental Zn with the same distribution of Mn in the nanoflakes, indicating the charge storage of Zn^{2+} ion in the δ-MnO_2 cathode. Surprisingly, the nondiffusion controlled "pseudocapacitive"-like Zn^{2+} ion storage in δ-MnO_2 has a high specific capacity (238.8 mAh g^{-1} at 0.2 C, 78% of theoretical capacity for 1e^- transfer). The high nondiffusion controlled capacity is in sharp contrast of the electrochemical capacitor that is commonly associated with the surface or near-surface redox reaction,[35] indicating Zn^{2+} insertion into the bulk structure of δ-MnO_2 instead of on the outer surface (Surface area: 34.08 m^2 g^{-1}; Figure S3, Supporting Information). The nondiffusion controlled Zn^{2+} intercalation could be related to the 2D crystal network of δ-MnO_2 that allows a fast transport pathway with little crystal phase change (To be discussed later).[33] Such phenomenon has also been observed for Li^+ intercalation pseudocapacitance in the bulk of 2D materials, such as T-Nb_2O_5.[33]

In addition, the anion species of zinc salt or manganese salt strongly affect the ion association properties in solutions. We find that the charge storage mechanism in layer δ-MnO_2 varies with electrolyte media for the redox relations (Figure S4, Supporting Information). The quantification of charge storage kinetic in δ-MnO_2 in 1 M $ZnSO_4$ and 0.1 M $MnSO_4$ electrolyte was performed in Figure S5 (Supporting Information). Similar mixed charge storage were observed in δ-MnO_2. However, the separation of two different charge storage processes is much more obvious in $ZnSO_4$-based electrolyte. At sweep rate < 1 mV s^{-1}, the charge storage kinetics in δ-MnO_2 is dominated by nondiffusion controlled charge storage with b value close to 1 (capacity contribution: ≈95%). While at sweep rate > 1 mV s^{-1}, the b approaches a value of 0.5 (Figure S5, Supporting Information).

Furthermore, it was found that the joint charge storage mechanism in δ-MnO_2 is less associated with the morphology of δ-MnO_2 rather than the electrolyte. Similar charge storage mechanism was observed for the δ-MnO_2 with different particle size and surface area (Figure S6, Supporting Information). Zinc salts with a bulky anion such as $TFSI^-$ and TF^-, seems to lead obviously to more nondiffusion controlled charge storage in δ-MnO_2 than that in the $ZnSO_4$-based electrolyte in the higher sweep rate range (Figures S7, S8, Supporting Information). δ-MnO_2 exhibits basically similar joint charge storage mechanism in electrolytes with different pH values as shown in Figure S9 (Supporting Information). Nevertheless, the pH value of electrolyte shows some modification on the joint charge storage mechanism in δ-MnO_2. Lower pH value seems to favor the nondiffusion controlled Zn^{2+} storage capacity in δ-MnO_2 under high sweep rate (Figure S9, Supporting Information). This could be because that the increasing of H^+ concentration frees some Zn^{2+} cation from coordinating with OH^- in water solution and facilitates its intercalation.[36]

To further understand the different charge storage mechanism, the structural evolution of δ-MnO_2 was carefully investigated during cycling. **Figure 4**a shows the charge and discharge curve of δ-MnO_2 and the selected charge–discharge status for ex-situ XRD measurements in the second cycle at 0.2 C (equals to < 1 mV s^{-1}) in 1 M $Zn(TFSI)_2$ electrolyte. Note that the ex-situ XRD for δ-MnO_2 electrodes were tested after disassembling the cell without rising by water. Interestingly, no new XRD peak showed up beside the peaks from $Zn(TFSI)_2$ salts (Figure S10, Supporting Information) in electrolyte before discharging to 1.43 V (Status I), indicating no visible crystal structure change of δ-MnO_2. The capacity before 1.43 V is, therefore, mainly produced by the nondiffusion controlled "pseudocapacitive"-like Zn^{2+} intercalation in the bulk δ-MnO_2 without a phase change,[33] which is consistent with the more closer *b* value to 1 for the reduction peak 1 in Figure 3b. Along with the discharge process, a set of new peaks (marked by yellow solid line) appear from the discharge voltage of 1.22 V (Status II), and the intensity continuously increases until the end of discharge to 1 V (Status IV) along with the gradual reduction in the peak intensity of δ-MnO_2 phase (marked by gray dashed line). The set of newly appeared peaks (marked by yellow solid line) likely belongs to $Zn(TFSI)_2[Zn(OH)_2]_3.xH_2O$ discharge product, which is an analogy of $ZnSO_4[Zn(OH)_2]_3.nH_2O$ (n = 3, 4 etc.) that was observed in Zn-MnO_2 batteries in $ZnSO_4$-based electrolytes (Figure S11, Supporting Information).[16] The presence of $Zn(TFSI)_2[Zn(OH)_2]_3.xH_2O$ in the δ-MnO_2 cathode indicates the H^+ conversion reaction with δ-MnO_2 to form MnOOH during further discharge process, which is evidenced by the XRD patterns of MnOOH as shown in Figure S12 (Supporting Information). Meanwhile, the OH^- reaction with the Zn^{2+} ion dissolved from Zn anode and $Zn(TFSI)_2$ aqueous electrolyte to form the accompanied discharge compound of $Zn(TFSI)_2[Zn(OH)_2]_3.xH_2O$ on δ-MnO_2 electrode along with the redox reaction of $MnO_2 + H \leftrightarrow MnOOH$, which is also evidenced by the SEM image of newly formed flakes in the δ-MnO_2 electrodes in discharged status (Figure S13a,

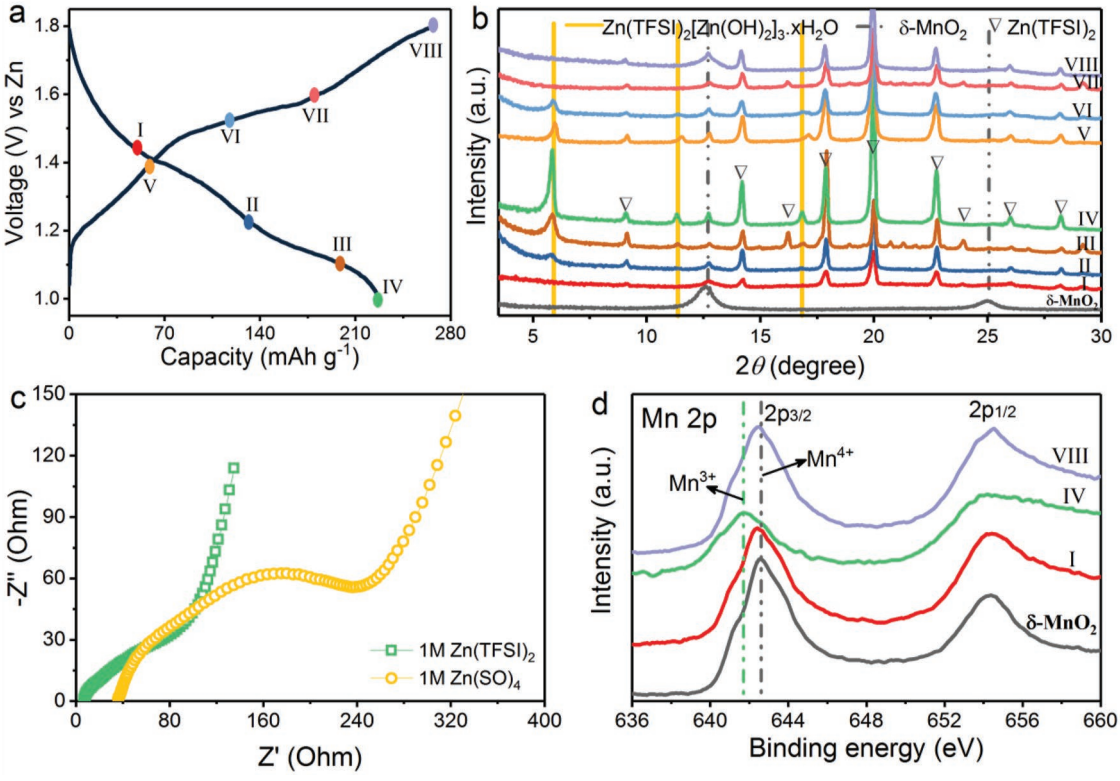

Figure 4. Joint nondiffusion controlled Zn^{2+} intercalation and H^+ conversion reaction mechanism. a) Charge–discharge curve δ-MnO_2 electrodes in the second cycle at 0.2 C. b) Ex-situ XRD patterns of δ-MnO_2 electrodes at selected states in (a). c) EIS analysis of Zn-δ-MnO_2 cells at discharged state. d) XPS spectra for Mn 2p at the selected states in (a). Electrolyte: 1 M $Zn(TFSI)_2$ electrolyte with 0.1 M $Mn(TFSI)_2$ additive in water.

Supporting Information). We further compared the XRD patterns of δ-MnO_2 electrodes after rising with DI-water at the end discharge state. The $Zn(TFSI)_2[Zn(OH)_2]_3.xH_2O$ peaks disappeared after complete rinse with water, indicating that formed $Zn(TFSI)_2[Zn(OH)_2]_3.xH_2O$ in δ-MnO_2 cathode is washable by water (Figure S11a, Supporting Information), which was confirmed by the disappearance of flake-like of $Zn(TFSI)_2[Zn(OH)_2]_3.xH_2O$ in the SEM image of δ-MnO_2 cathode at the discharge state of 1 V after DI-water rinse (Figure S13b, Supporting Information). In contrast, the $ZnSO_4[Zn(OH)_2]_3.nH_2O$ formed in δ-MnO_2 cathode in $ZnSO_4$-based electrolyte is not soluble in water and remains without change in XRD patterns before and after rinsing (Figure S11b, Supporting Information). Therefore, δ-MnO_2 electrode in $Zn(TFSI)_2$-based electrolyte leads to both low ohm resistance and interfacial charge transfer ~3 times lower than that in $ZnSO_4$-based electrolyte (Figure 4c), which would further benefit the rate capability of δ-MnO_2 cathode.

The charge process is highly reversible in the charge–discharge process. As charge voltage increased, the peak intensity of $Zn(TFSI)_2[Zn(OH)_2]_3.xH_2O$ gradually decreased (Status V, VI), and reversibly disappeared at the charge voltage of 1.6 V (Status VII). Between the charges voltages of 1.6 and 1.8 V, the XRD peaks did not change significantly for δ-MnO_2 phase except for the gradual intensity increase. This indicates that the capacity observed in this high charge voltage range is from the extraction of nondiffusion controlled Zn^{2+} ions storage in the bulky structure of δ-MnO_2 phase with no obvious crystal structure change. No large flake-like $Zn(TFSI)_2[Zn(OH)_2]_3.xH_2O$ was observed in δ-MnO_2 electrode charge to 1.8 V (Figure S13d, Supporting Information), confirming the reversible formation and decomposition of $Zn(TFSI)_2[Zn(OH)_2]_3.xH_2O$ during cycling.

The X-ray photoelectron spectroscopy (XPS) analysis for Mn $2p_{3/2}$ peaks in δ-MnO_2 electrodes reveals the valance status change of Mn during charge and discharge in Figure 4d. The $Mn2p_{3/2}$ peaks for δ-MnO_2 at discharge status I exhibit a dominated peak at 642.5 eV with a shoulder at 641.6 eV, which are ascribed to the existence of Mn^{4+} and Mn^{3+}, respectively, in δ-MnO_2 electrode after initial Zn^{2+} intercalation. The Mn $2p_{3/2}$ peak significantly shifted to the lower binding energy with a dominated reduced peak of Mn^{3+} (641.6 eV) at the end of discharge (state IV);[37] and it changed back to the original binding energy in the charge process (state VIII) along with the Mn oxidized to its initial state. The reversible valence status change for Mn 2p further confirms the reversible joint charge storage in δ-MnO_2 structure.

TEM images were further used to investigate the morphological and structural evolution of δ-MnO_2 electrode at lattice-scale during the charge–discharge process in 1 M $Zn(TFSI)_2$-based electrolyte in the first cycle. **Figure 5**a–c shows the TEM/HRTEM images of δ-MnO_2 electrode at the discharge state of 1 V. It was found that the pristine flake-like δ-MnO_2 particles were transformed into two kinds of crystal morphologies at

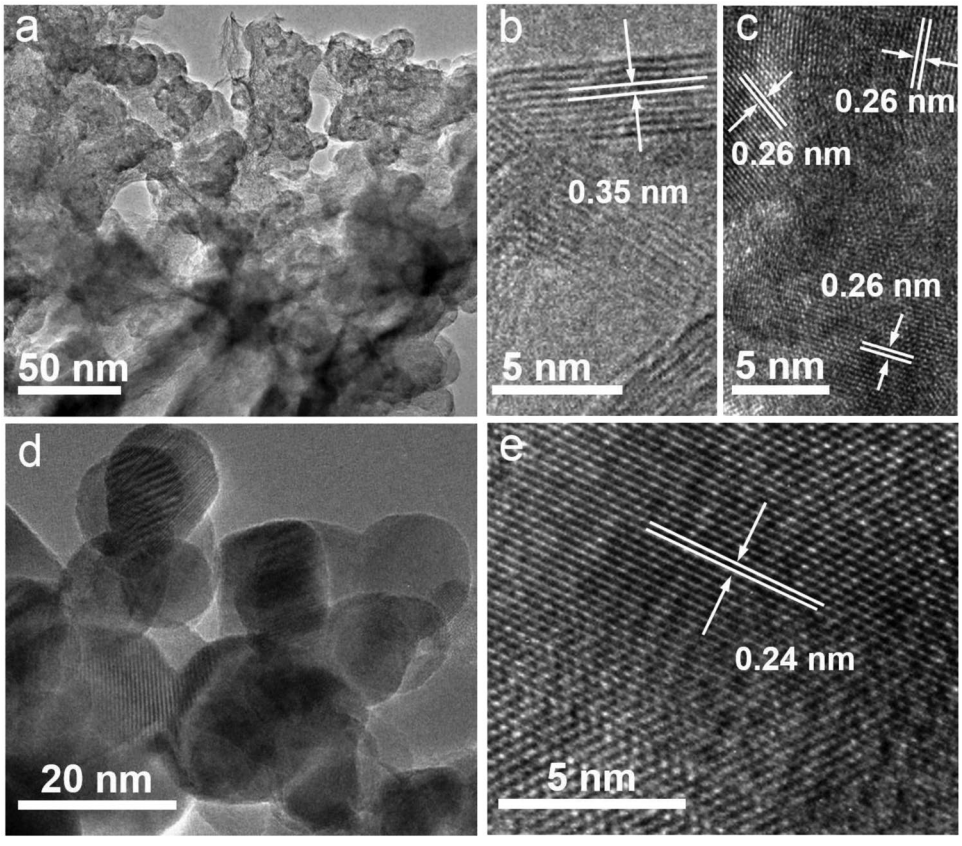

Figure 5. TEM images of δ-MnO_2 electrodes during the electrochemical process. a–c) MnO_2 electrodes discharged to 1 V. d, e) MnO_2 electrodes charged back to 1.8 V. (first cycle). Electrolyte: 1 M $Zn(TFSI)_2$ electrolyte with 0.1 M $Mn(TFSI)_2$ additive in water.

higher magnification. The nanoflake like morphology with lattice distance of 0.35 nm corresponds to the (0 0 2) plane of δ-MnO_2 (Figure 5b). This well-preserved nanoflakes further confirm the nondiffusion controlled "pseudocapacitance"-like Zn^{2+} intercalation in bulk δ-MnO_2 without phase change,[33] which is consistent with ex-situ XRD results in Figure 4b. The other main morphology is the ≈ 5 nm nanoparticle aggregates with some disorder in crystals as demonstrated in the HRTEM of Figure 5c. The lattice distance of 0.26 nm in nanoparticles aggregates corresponds to the (0 4 0) planes of MnOOH phase, as evidenced by the XRD in Figure S12 (Supporting Information). The appearance of MnOOH confirms the proton reactions with δ-MnO_2. The two different morphologies after first discharge could modify the reaction kinetics for the Zn^{2+} intercalation and phase change conversion reaction with H^+ in the following cycles due to the reduced diffusion length in nanoparticle for the reaction between MnO_2 and H^+ to form MnOOH. Furthermore, the morphology was converted into the crystal particle at the fully charged state of 1.8 V (Figure 5d). The HRTEM images indicate that the lattice distance of 0.24 nm is the (−1 1 1) plane of the original δ-MnO_2 electrode (Figure 5e), revealing the reversible crystal structural change of δ-MnO_2.

The structural and chemical evolution of δ-MnO_2 during charge and discharge process confirms the charge storage mechanisms in δ-MnO_2 and reveals the reaction sequence between nondiffusion controlled Zn^{2+} intercalation and H^+ conversion reaction in δ-MnO_2. The reaction mechanism and charge storage sequence are mainly manipulated by the electrolyte media, and also depends on charge–discharge current rates. During the discharge process, nondiffusion controlled Zn^{2+} intercalation in bulk δ-MnO_2 first occurs and dominates the high voltage discharge process, and the H^+ conversion reaction with MnO_2 dominantly takes place in the further discharge process under a medium charge rate as illustrated in Figure 1. Note that the specific charge storage process could vary under high C-rates. For the charge process, it is highly reversible with H^+ conversion reaction at the early charge stage and nondiffusion controlled Zn^{2+} intercalation at the high voltage charge process. This joint charge storage in δ-MnO_2 with appropriate electrolyte media, such as $Zn(TFSI)_2$-based electrolyte, facilitates fast charge storage kinetics and accounts for the observed high rate capability of δ-MnO_2 in the appropriate electrolyte as discussed in Figure 3.

The overall reactions for Zn-δ-MnO_2 batteries in $Zn(TFSI)_2$-based electrolyte can be the following processes during charge and discharge

Cathode:

$$MnO_2 + xZn^{2+} + 2xe^- \leftrightarrow Zn_xMnO_2 (\text{Nondiffusion} - \text{controlled reaction}) \quad (1)$$

$$H_2O \leftrightarrow H^+ + OH^- \quad (2)$$

$$MnO_2 + H^+ + e^- \leftrightarrow MnOOH (\text{Diffusion} - \text{controlled reaction}) \quad (3)$$

$$\frac{1}{2}Zn^{2+} + OH^- + \frac{1}{6}Zn(TFSI)_2 + \frac{x}{6}H_2O \leftrightarrow \frac{1}{6}Zn(TFSI)_2[Zn(OH)_2]_3 \cdot xH_2O \quad (4)$$

Anode:

$$\left(\frac{1}{2}+x\right)Zn \leftrightarrow \left(\frac{1}{2}+x\right)Zn^{2+} + (1+2x)e^- \quad (5)$$

The electrochemical properties of layered δ-MnO_2 were then evaluated in coin cells using δ-MnO_2 as the cathode and Zn metal as the anode in different electrolytes. δ-MnO_2 cathode shows excellent rate performance, demonstrating high discharge capacities of 238, 220, 171, and 138 mAh g^{-1} at 0.2 C, 1 C, 5 C, and 20 C, respectively, in 1 M $Zn(TFSI)_2$ with 0.1 M $Mn(TFSI)_2$ electrolyte (**Figure 6**a). (Note that the relatively low current rate, e.g. 0.2 C, will cause more of oxidation of preaddition of Mn^{2+} additive in electrolyte than the dissolution of Mn^{2+} from electrode during the slow charging process, leading to lower Coulombic efficiency at low current rate). The charge–discharge capacity exhibits less obvious decrease under 1 C rate, showing that the ion-diffusion is not a rate-limiting step for charge storage. In contrast, the rate capability of δ-MnO_2 cathode deteriorates a lot in $ZnSO_4$-based electrolyte with increased overpotential and reduced capacity utilization even though the same δ-MnO_2 cathode was used (Figure S14, Supporting Information). The improved performance of δ-MnO_2 could be likely ascribed to excellent kinetics of nondiffusion controlled Zn^{2+} ion intercalation in the bulk of the nanoflake-like δ-MnO_2 electrodes during charge and discharge processes in $Zn(TFSI)_2$-based electrolyte in a wide C rate range. This is consistent with the kinetics of charge storage in layered δ-MnO_2

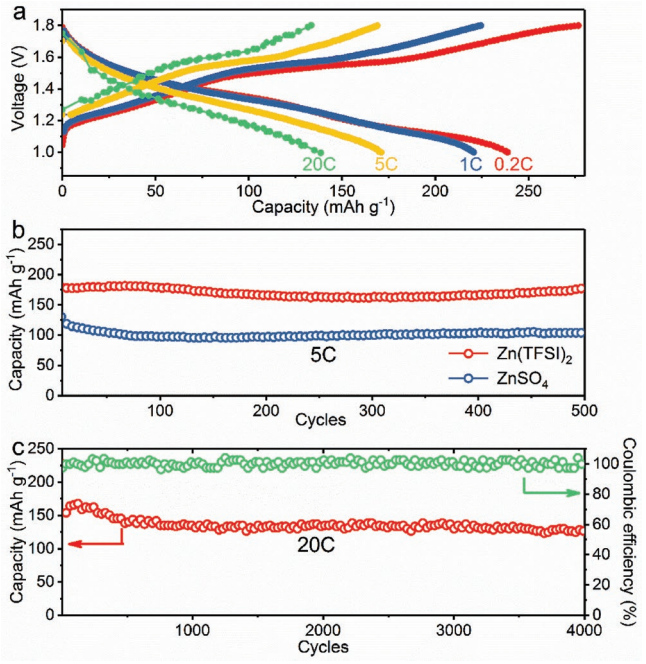

Figure 6. The electrochemical performance of Zn-δ-MnO_2 batteries. a) Rate performance of Zn- δ-MnO_2 battery in 1 M $Zn(TFSI)_2$ with 0.1 M $Mn(TFSI)_2$ additive electrolyte. b) Comparison of the cycling performance of δ-MnO_2 electrodes at 5 C in 1 M $Zn(TFSI)_2$ with 0.1 M $Mn(TFSI)_2$ additive and 1 M $ZnSO_4$ with 0.1 M $MnSO_4$ electrolyte, respectively. c) The long cycle performance of Zn- δ-MnO_2 battery at 20 C in 1 M $Zn(TFSI)_2$ with 0.1 M $Mn(TFSI)_2$ additive electrolyte.

as discussed in Figure 3 and the low charge transfer impedance in Figure 4c. The manipulation of redox reactions in δ-MnO_2 cathode via reaction media provides a new gateway to design high rate and high energy batteries systems beyond the modification of electrode material itself. In addition, the Zn-MnO_2 battery also demonstrates higher cycling stability with higher capacity in $Zn(TFSI)_2$-based electrolyte than that in $ZnSO_4$ electrolyte at 5 C (Figure 6b). Excellent long-cycle stability at high operation rate of 20 C was shown, with a discharge capacity of 136.9 mAh g^{-1} and high-capacity retention of 93% over 4000 cycles (Figure 6c). The combination of superior high-rate performance, long cycle life, environmentally friendly and low cost of electrode materials in Zn-MnO_2 batteries enables an excellent alternative solution for energy storage. In addition, the Zn anode also exhibits good stability in the $Zn(TFSI)_2$-based electrolyte with a stabilized Coulombic efficiency of >99% over thousand cycles under shallow plating/stripping as shown in Figure S15 (Supporting Information). However, approaches to improve the stability and reversibility of Zn anode under higher utilization is still critical for the practical application.

In summary, we demonstrate a new charge storage mechanism in δ-MnO_2 for designing high-rate performance Zn-MnO_2 batteries. A joint nondiffusion controlled Zn^{2+} intercalation in bulk δ-MnO_2 and H^+ conversion reaction pathway was identified in δ-MnO_2 cathode during charge and discharge, in which the charge storage mechanisms could be tailored through electrolytes, especially via the anion of zinc salt. Fast reaction kinetics not limited by ion diffusion was realized for Zn-δ-MnO_2 batteries in $Zn(TFSI)_2$-based mild aqueous electrolyte in a wide C-rate range. This mixed energy storage mechanism contributes to superior high rate electrochemical performance of 136.9 mAh g^{-1} discharge capacity at 20 C and 93% capacity retention after 4000 cycles. This study opens a new gateway to the design of high-rate electrode materials by manipulating the effective redox reactions in electrode materials for rechargeable batteries.

Experimental Section

Material Synthesis: δ-MnO_2 was synthesized by hydrothermal method. $KMnO_4$ and $MnSO_4$ with a molar ratio of 6:1 were put into a beaker and stirred to make the reactant totally dissolved. The solution was put into a Teflon contained autoclave and heated at 160 °C for 12 h. The solution was then cooled to room temperature. δ-MnO_2 powder was obtained through the centrifuge, washed with deionized water three times, and dried at 60 °C overnight.

Characterizations: XRD measurements were performed using a Rigaku Miniflex II diffractometer with Cu Kα radiation (λ = 1.5406 Å). SEM was obtained on Helium ion microscope. Transition electron microscopy (TEM) images were conducted on FEI Titan at 300 kV. XPS measurements were performed using a Physical Electronics Quantera Scanning X-ray Microprobe. The specific surface area of δ-MnO_2 powder was determined by nitrogen adsorption curve, which was conducted on the surface area analyzer (Quantachrome, USA) and estimated by BET (Brunauer–Emmett–Teller) method.

Electrochemical Measurements: δ-MnO_2 was mixed with acetylene black and PVDF with a weight ratio of 6:3:1 in NMP solvent. The slurry was spread on carbon paper current collector and heated at 80 °C under vacuum condition overnight. The electrode was punched into 0.5 inch diameter disc and mass loading was around 1 mg cm^{-2}. 2023 coin cell was assembled to evaluate the electrochemical performance of δ-MnO_2 with Zn foil (Alfa Aesar) as counter electrode and glass fiber as the separator. The galvanostatic charge/discharge was carried out in the voltage range of 1–1.8 V on a LANHER battery tester (Wuhan). Cyclic voltammetry (CV) measurements were conducted using CHI660E. Electrochemical impedance spectra (EIS) were performed on Bio-Logic Instruments (VSP) using a three-electrode cell configuration with δ-MnO_2 as the working electrode and Zn metal as both reference and counter electrodes.

Supporting Information

Supporting Information is available from the Wiley Online Library or from the author.

Acknowledgements

This work was supported by the U.S. Department of Energy (DOE), Office of Basic Energy Sciences, Division of Materials Sciences and Engineering, under Award KC020105-FWP12152 for the design and execution of experiments. Y.J. acknowledges the China Scholarship Council (CSC) scholarship for supporting to complete the project research. The SEM, TEM, and STEM analyses were performed in the William R. Wiley Environmental Molecular Sciences Laboratory, a national scientific user facility sponsored by the DOE Office of Biological and Environmental Research and located at PNNL. PNNL is a multiprogram national laboratory operated for DOE by Battelle.

Conflict of Interest

The authors declare no conflict of interest.

Keywords

Aqueous Zn-MnO_2 batteries, high-rate batteries, joint charge storage, battery reaction mechanisms

Received: January 23, 2019
Revised: April 16, 2019
Published online: June 3, 2019

[1] B. Dunn, H. Kamath, J.-M. Tarascon, *Science* **2011**, *334*, 928.
[2] S. Chu, A. Majumdar, *Nature* **2012**, *488*, 294.
[3] J. Liu, J. G. Zhang, Z. Yang, J. P. Lemmon, C. Imhoff, G. L. Graff, L. Li, J. Hu, C. Wang, J. Xiao, *Adv. Funct. Mater.* **2013**, *23*, 929.
[4] D. Larcher, J.-M. Tarascon, *Nat. Chem.* **2015**, *7*, 19.
[5] S. Chu, Y. Cui, N. Liu, *Nat. Mater.* **2017**, *16*, 16.
[6] J. Rugolo, M. J. Aziz, *Energy Environ. Sci.* **2012**, *5*, 7151.
[7] W. Wei, X. Cui, W. Chen, D. G. Ivey, *Chem. Soc. Rev.* **2011**, *40*, 1697.
[8] L. L. Zhang, X. Zhao, *Chem. Soc. Rev.* **2009**, *38*, 2520.
[9] P. Simon, Y. Gogotsi, *Nat. Mater.* **2008**, *7*, 845.
[10] V. Augustyn, P. Simon, B. Dunn, *Energy Environ. Sci.* **2014**, *7*, 1597.
[11] S.-L. Kuo, N.-L. Wu, *J. Electrochem. Soc.* **2006**, *153*, A1317.
[12] Z. Fan, J. Yan, T. Wei, L. Zhi, G. Ning, T. Li, F. Wei, *Adv. Funct. Mater.* **2011**, *21*, 2366.
[13] Z. S. Wu, K. Parvez, X. Feng, K. Müllen, *Nat. Commun.* **2013**, *4*, 2487.
[14] M. Song, H. Tan, D. Chao, H. J. Fan, *Adv. Funct. Mater.* **2018**, *28*, 1802564.

[15] J. Huang, Z. Wang, M. Hou, X. Dong, Y. Liu, Y. Wang, Y. Xia, *Nat. Commun.* **2018**, *9*, 2906.
[16] H. Pan, Y. Shao, P. Yan, Y. Cheng, K. S. Han, Z. Nie, C. Wang, J. Yang, X. Li, P. Bhattacharya, *Nat. Energy* **2016**, *1*, 16039.
[17] W. Sun, F. Wang, S. Hou, C. Yang, X. Fan, Z. Ma, T. Gao, F. Han, R. Hu, M. Zhu, *J. Am. Chem. Soc.* **2017**, *139*, 9775.
[18] N. Zhang, F. Cheng, J. Liu, L. Wang, X. Long, X. Liu, F. Li, J. Chen, *Nat. Commun.* **2017**, *8*, 405.
[19] S.-D. Han, S. Kim, D. Li, V. Petkov, H. D. Yoo, P. J. Phillips, H. Wang, J. J. Kim, K. L. More, B. Key, *Chem. Mater.* **2017**, *29*, 4874.
[20] J. Ding, Z. Du, L. Gu, B. Li, L. Wang, S. Wang, Y. Gong, S. Yang, *Adv. Mater.* **2018**, *30*, 1800762.
[21] D. Kundu, B. D. Adams, V. Duffort, S. H. Vajargah, L. F. Nazar, *Nat. Energy* **2016**, *1*, 16119.
[22] F. Wan, L. Zhang, X. Dai, X. Wang, Z. Niu, J. Chen, *Nat. Commun.* **2018**, *9*, 1656.
[23] R. Trócoli, F. La Mantia, *ChemSusChem* **2015**, *8*, 481.
[24] L. Zhang, L. Chen, X. Zhou, Z. Liu, *Adv. Energy Mater.* **2015**, *5*, 1400930.
[25] N. Zhang, F. Cheng, Y. Liu, Q. Zhao, K. Lei, C. Chen, X. Liu, J. Chen, *J. Am. Chem. Soc.* **2016**, *138*, 12894.
[26] G. Li, Z. Yang, Y. Jiang, C. Jin, W. Huang, X. Ding, Y. Huang, *Nano Energy* **2016**, *25*, 211.
[27] C. Xu, B. Li, H. Du, F. Kang, *Angew. Chem.* **2012**, *124*, 957.
[28] M. H. Alfaruqi, J. Gim, S. Kim, J. Song, D. T. Pham, J. Jo, Z. Xiu, V. Mathew, J. Kim, *Electrochem. Commun.* **2015**, *60*, 121.
[29] B. Lee, H. R. Lee, H. Kim, K. Y. Chung, B. W. Cho, S. H. Oh, *Chem. Commun.* **2015**, *51*, 9265.
[30] M. H. Alfaruqi, V. Mathew, J. Gim, S. Kim, J. Song, J. P. Baboo, S. H. Choi, J. Kim, *Chem. Mater.* **2015**, *27*, 3609.
[31] G. G. Yadav, J. W. Gallaway, D. E. Turney, M. Nyce, J. Huang, X. Wei, S. Banerjee, *Nat. Commun.* **2017**, *8*, 14424.
[32] G. Du, J. Wang, Z. Guo, Z. Chen, H. Liu, *Mater. Lett.* **2011**, *65*, 1319.
[33] V. Augustyn, J. Come, M. A. Lowe, J. W. Kim, P.-L. Taberna, S. H. Tolbert, H. D. Abruña, P. Simon, B. Dunn, *Nat. Mater.* **2013**, *12*, 518.
[34] T. C. Liu, W. Pell, B. Conway, S. Roberson, *J. Electrochem. Soc.* **1998**, *145*, 1882.
[35] Y. Liu, F. Zhou, V. Ozolins, *J. Phys. Chem. C* **2012**, *116*, 1450.
[36] A. K. Katz, J. P. Glusker, S. A. Beebe, C. W. Bock, *J. Am. Chem. Soc.* **1996**, *118*, 5752.
[37] F. Zeng, Y. Pan, Y. Yang, Q. Li, G. Li, Z. Hou, G. Gu, *Electrochim. Acta* **2016**, *196*, 587.